ACS Catalysis

pubs.acs.org/acscatalysis Research Article

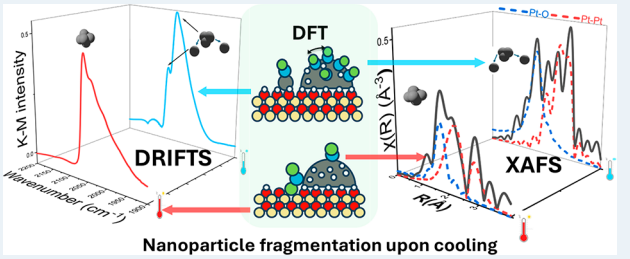
Low-Temperature Catalyst Redispersion: A Route to Enhanced Stability of Supported Metal Catalysts?

Rafat H. Aunkon, Hyuk Choi, Ryuichi Shimogawa, Haodong Wang, Lihua Zhang, Christian Reece, Yuanyuan Li, Hyun You Kim, and Anatoly I. Frenkel*

Cite This: *ACS Catal.* 2025, 15, 19709−19720 Read Online

ACCESS | Metrics & More | Article Recommendations | Supporting Information

ABSTRACT: Sintering poses a significant challenge to achieving the long-term stability of supported metal catalysts under reaction conditions. Here, we report a low-temperature catalyst redispersion mechanism, in which platinum single atoms, which aggregate into nanoparticles under Reverse Water Gas Shift (RWGS) conditions at elevated temperatures, fragment into atomically dispersed species upon cooling. Using multimodal operando characterization combined with first-principles theoretical modeling, we track the structural evolution of Pt single atoms supported on ceria nanodomes, deposited either on ceria or ceria−titania mixed oxides. We find that fragmentation is more pronounced when cooling occurs under RWGS conditions compared to CO alone, owing to a synergistic interplay of the effects of H_2, CO_2, and CO. The support architecture has a strong influence on the extent of redispersion: while CO alone induces fragmentation on ceria, interfacial confinement and vacancy pinning at the ceria−titania interface suppress restructuring. In contrast, RWGS conditions overcome these barriers, enabling redispersion across both supports. These findings point toward a pathway for catalyst stabilization via reaction-induced redispersion under mild conditions.



KEYWORDS: *reaction-driven redispersion, single-atom catalysts, reverse water gas shift reaction, In-situ, catalyst-restructuring*

Downloaded via STONY BROOK UNIV SUNY on November 12, 2025 at 19:26:55 (UTC).
See https://pubs.acs.org/sharingguidelines for options on how to legitimately share published articles.

INTRODUCTION

Over more than a decade of work with atomically dispersed catalysts, many examples of their enhanced activity,[1,2] selectivity,[3,4] and new catalytic pathways[5,6] have been demonstrated. One problem that remains unsolved is overcoming the relatively poor thermodynamic stability of single atom catalysts (SACs), particularly under high temperature and reducing environments, which are common to many heterogeneously catalyzed reactions.[7−11] A common outcome is sintering—a primary cause of catalyst deactivation.[12,13]

A range of strategies has been developed to enhance the resistance of nanostructures to thermally induced sintering.[14,15] For instance, aliovalent-doped CeO_2 has higher oxygen vacancies that can anchor Pt atoms, limiting their agglomeration to higher temperatures than on undoped CeO_2.[15] Other reported strategies range from the use of overcoating metals with oxides or carbon layers,[16] which act as diffusion barriers, to spatial confinement within mesoporous structures such as carbon nanotubes,[17] zeolites,[18] and MOFs.[19] However, these methods often introduce trade-offs as confinement limits mass transport, compromising catalytic activity and selectivity.[20]

A plausible alternative to the kinetic stabilization of catalysts from sintering, summarized above, can be found in the phenomenon of nanoparticle redispersion. It was shown to preserve high activity and selectivity for metal catalysts based on Pt,[21−23] Pd,[24] and Rh.[25−27] One widely studied mechanism is the oxidation−mobilization−reduction route.[21,24,25] Following that route upon oxidation, metal aggregates transform into mobile oxy-species that migrate across the catalyst surface. However, this method is constrained by temperature sensitivity and material-specific behavior. For instance, Rhodium-based systems such as Rh/CeO_2 and $RhVO_4/SiO_2$ require reoxidation at extremely high temperatures (800−900 °C) for effective redispersion.[25,26] In contrast, $Pt−Sn/Al_2O_3$ catalysts exhibit a different limitation: while redispersion can be initially induced through successive oxidation−reduction cycles, these cycles ultimately promote platinum sintering, thereby diminishing the effectiveness of redispersion over time.[28] Notably, in Pt/Al_2O_3 systems, oxidation may disrupt the metal lattice without fragmenting the particles. Subsequent reduction can induce fissures that increase the surface area, even though the overall particle size remains largely unchanged.[29]

Another widely explored method is oxychlorination-based redispersion.[23,30] For 0.6 wt % Pt, 0.9 wt % Cl Pt/γ-Al_2O_3

Received: August 27, 2025
Revised: October 29, 2025
Accepted: November 5, 2025

© XXXX American Chemical Society

https://doi.org/10.1021/acscatal.5c06004
ACS Catal. 2025, 15, 19709−19720

catalyst, Monzón et al. demonstrated that the oxychlorination treatment at 773 K using $HCl/O_2/H_2O/N_2$ led to an enhanced Pt dispersion, attributed to the formation of highly mobile $[Pt(OH)_4Cl_2]^{2-}$ species.[31] Likewise, in Pt/Al_2O_3 systems, redispersion at 500−600 °C has been linked to the formation of $Pt^{IV}O_xCl_y$ intermediates.[32] However, despite its effectiveness, oxychlorination requires the presence of chlorine, either in the catalyst or the treatment environment, which raises significant environmental and operational concerns.

Recognizing these limitations, recent efforts have shifted toward developing dynamic redispersion strategies. In this context, reports of reversible, ligand-mediated redispersion of Rh nanoparticles have emerged as promising advances.[33−35] For example, Yan et al. found in Rh/CeO_2 catalysts, Rh single atoms sinter into nanoparticles upon H_2 pretreatment at 500 °C; however, during steam reforming of methane ($CH_4 + H_2O \rightarrow CO + 3H_2$) at the same temperature, the in situ generated CO induces the fragmentation of Rh nanoparticles into sub nanometer $Rh_3(CO)_n$ clusters that under CH_4 steam reforming, and eventually $Rh_1(CO)_2$ single atoms anchored at CeO_2 defect sites.[33] Similarly, Matsubu et al. reported that in CO_2-rich, H_2-lean RWGS conditions at 200 °C, adsorbed CO and H_2O destabilize Rh bonds on TiO_2, causing atom detachment and reanchoring as isolated single-atom sites at surface defects.[34] In these works, however, redispersion was obtained during high-temperature reaction conditions. In this article, we explore an alternative strategy for catalyst redispersion relying on a process in which the fragmentation, or redispersion of the catalyst, occurs upon its deactivation while cooling down from catalytic active state.

In our previous work,[36] we observed that Pt nanoparticles partially fragment into isolated single atoms on support upon cooling to room temperature in the presence of carbon monoxide (CO), and this process is reversible (single atoms reassemble into nanoparticles at elevated temperatures and in reverse water gas shift reaction conditions). We have elucidated the underlying mechanism by theoretical modeling, revealing that hydrogen promotes Pt aggregation, whereas a combination of strong repulsive CO−CO and attractive Pt−CO interactions drive fragmentation. However, a comprehensive understanding of the fragmentation mechanism in this ubiquitous catalytic system should be based not only on the individual factors, which were investigated in most prior studies, including ours,[36] but on their complex interactions accompanying a real chemical reaction. The chief among them are the effects of temperature, gas composition, adsorbate dynamics, and metal−metal and metal−support interactions.[37−42] Also, the observation of such redispersion that was first observed upon cooling in a CO-rich environment was serendipitous, because the most significant interest is in the stability of the catalyst in operating conditions, i.e., at high temperature and in a reaction environment. Only through a deliberate, systematic investigation of the factors responsible for fragmentation during cooling can one design a series of controlled experiments aimed at disentangling the competing influences that collectively drive the fragmentation and redispersion of Pt systems.

In that regard, this study addresses a central question: How can the effects of Pt-adsorbate, Pt−Pt, and Pt-support interactions be quantified for understanding the fragmentation phenomena? To answer it, one needs the ability to tune those interactions by design of the reaction conditions and experimental system. We use Reverse Water Gas Shift (RWGS) reaction over supported Pt nanoparticles, which involves simultaneous exposure to H_2 and CO—two key species known for influencing metal − metal and metal−support interactions.[43−45] For tuning the Pt-support interaction, in addition to varying the reaction temperature and gas atmospheres (e.g., changing the conditions between the RWGS and pure CO), we also vary the support (pure CeO_2 and mixed, CeO_2−TiO_2). To decouple these entangled interactions, we employed multimodal, correlative experiments. Here, in situ Diffuse Reflectance Infrared Fourier Transform Spectroscopy (DRIFTS) was employed to evaluate how different reactive environments influence Pt catalyst restructuring, leveraging CO as a dynamic probe to monitor surface coordination environments under varying thermal and adsorptive conditions. In situ X-ray Absorption Fine Structure (XAFS) spectroscopy provided complementary, quantitative insights into the local structure of Pt species. In addition, ex situ High-angle Annular Dark-Field Scanning Transmission Electron Microscopy (HAADF-STEM) was employed to elucidate the distribution and local structure of Pt species on supports. Complementary Density Functional Theory (DFT) calculations were performed to gain atomic-level insights into the roles of metal−metal, metal−adsorbate and metal−support interactions under reaction conditions.

MATERIALS AND METHODS

Sample Preparation. The catalyst was synthesized using wet impregnation method as reported previously,[8,15,46] resulting in 1 wt % Pt on ceria nanodomes that, in turn, were located on either CeO_2 (labeled as PCC) or TiO_2 supports (labeled as PCT). The samples were prepared by dispersing 0.5 g cerium(IV) oxide nanopowder (<25 nm) or titanium(IV) oxide nano powder (<25 nm) in a solution of 0.42 g of cerium(III) nitrate hexahydrate, 2.0 g urea and 8 mL of water. The weight loading of Pt was controlled by adding the desired amount of Pt precursor solution (chloroplatinic acid hydrate in water, approximately 1 wt % Pt) in each system. All chemicals were purchased from Sigma-Aldrich. Ultrapure water was provided by a Millipore purification system. The mixture was sealed in a glass vial and stirred for 24 h in an oil bath at 90 °C. Afterward, the samples were washed with DI water and centrifuged three times. After drying overnight in an oven at 80 °C, the samples were crushed into powders and calcined at 500 °C (5 °C/min heating ramp) for 5 h. The resulting platinum loadings of all samples were measured by inductively coupled plasma optical emission spectrometry (ICP-OES) by Galbraith Laboratories. The instrument measures characteristic emission spectra by optical spectrometry and describes multielemental determinations. Following synthesis and calcination, Pt was atomically dispersed on the ceria nanodomes, which were themselves supported either on ceria (PCC) or on titania (PCT). Under reducing conditions—either Reverse Water Gas Shift (RWGS) reaction environments (H_2 + CO_2) or pure H_2 at elevated temperature—the initially isolated Pt atoms aggregated into metallic nanoparticles. These aggregated states formed the starting point for subsequent cooling-phase experiments, where structural evolution and potential redispersion were probed under various reactive atmospheres.

Diffuse Reflectance Infrared Fourier Transform Spectroscopy (DRIFTS). The spectra were collected using a Thermo-Nicolet iS50 FTIR spectrometer equipped with a rapid-scanning option, liquid-nitrogen-cooled mercury cadmi-

https://doi.org/10.1021/acscatal.5c06004
ACS Catal. 2025, 15, 19709−19720

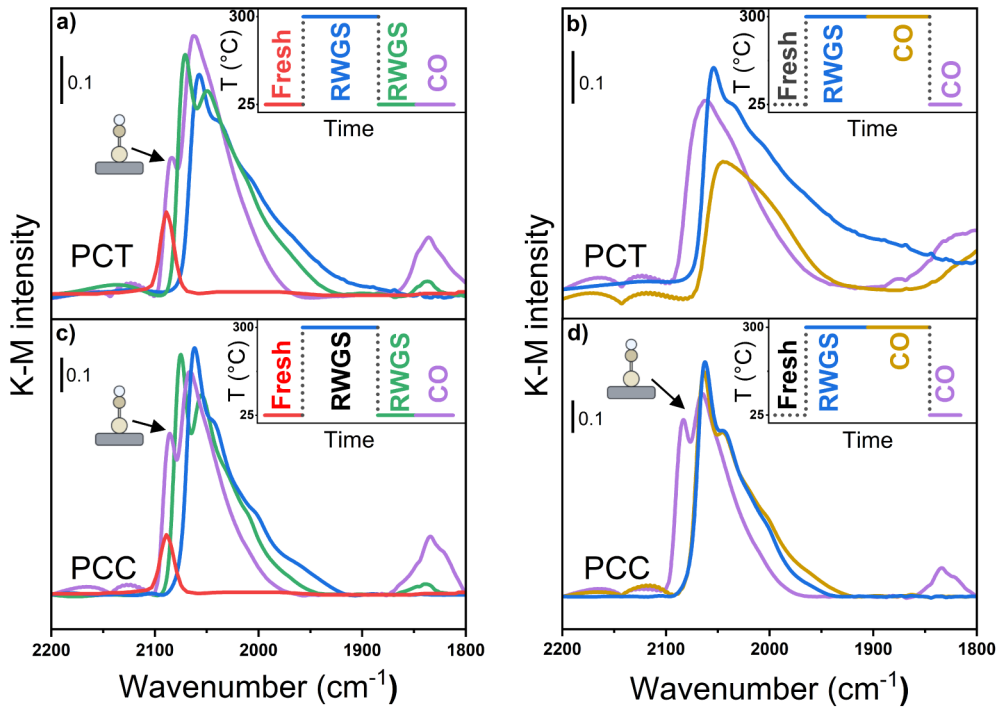


Figure 1. CO−DRIFTS spectra of PCT and PCC during RWGS at 300 °C followed by cooling under RWGS (a, c) or CO (b, d) atmospheres. The feature shown by an arrow in a), c), and d) indicates the presence of atomically dispersed Pt.

um telluride (MCT) detector, and a Praying Mantis High Temperature Reaction Chamber (Harrick Scientific Products). Approximately 15 mg of sample was loaded into the standard Harrick cup; a thin quartz-wool plug beneath the bed minimized dead volume. Prior to measurement, each sample was heated at 150 °C for 30 min under He with a flow rate of 20 mL/min to remove surface adsorbed species. Afterward, the background spectrum was collected under He with a flow rate of 20 mL/min at room temperature. The sample was exposed to a mixture of 5% CO_2 and 5% H_2 (balanced with He, with a total flow rate of 31.5 mL/min) at 300 °C to collect RWGS spectra. After that, the sample was cooled down to room temperature and collected RT spectra. For cooling down at CO, a mixture of 5% CO (balanced with He, the flow rate is 31.5 mL/min) was flowed through the reaction chamber to acquire CO adsorption spectra. Under each condition, the spectra were continuously collected until it reached steady state. Each DRIFTS spectrum (256 scans) was collected with a resolution of 4 cm^{-1}.

X-ray Absorption Spectroscopy (XAS). XAS measurements were performed at the QAS beamline (7-BM) of National Synchrotron Light Source II (NSLS II), Brookhaven National Laboratory. For in situ measurement, the sample was prepared in a pellet using a hydraulic press and mounted in a Nashner-Adler cell. In-situ data were collected at the indexed regions of time−temperature diagram at Figure S4a. At each regime, 30 scans of XAS data at the Pt L_3 edge were collected in fluorescence mode. The gas mixture of each regime is shown in TableS2.

High-Angle Annular Dark Field−Scanning Transmission Electron Microscopy (HAADF-STEM). HAADF-STEM imaging was carried out on Hitachi HD2700 STEM equipped with a probe aberration corrector, at Center for Functional Nanomaterials, Brookhaven National Laboratory. The powder sample was deposited onto a 3 mm Cu grid covered with an ultrathin carbon layer.

Density Functional Theory. We optimized the $CeO_2(100)$ surface using a 4 × 4 supercell with two O−Ce−O layers to describe the ceria nanoparticles in the experimental catalyst system. A vacuum layer was applied to 15Å to avoid electronic interference between the periodic supercells. We performed spin-polarized DFT calculations using a plane-wave basis with the VASP code[47,48] and the Perdew−Burke−Ernzerhof (PBE)[49] functional. The DFT+U scheme[50] with U_{eff} = 4.5 eV[51−53] was applied to Ce ions to accurately consider the localized Ce-*f* orbitals. The projector-augmented wave method[54] described the interaction between the ionic core and the valence electrons. Valence electron wave functions were expanded on a plane-wave basis up to an energy cutoff of 400 eV. The Brillouin zone was sampled at the *G*-point for all calculations. The convergence criteria for the electronic structure and the atomic geometry were 10^{-4} eV and 0.03 eV/Å, respectively. We used a Gaussian smearing function with a finite temperature width of 0.05 eV to improve the convergence of states near the Fermi level. The location and energy of transition states (TSs) were calculated using the climbing-image nudged-elastic-band method.[55,56]

RESULTS AND DISCUSSION

Reactive Environment-Dependent Pt Fragmentation in PCC and PCT as Probed by CO DRIFTS. To systematically evaluate the effects of reactive gases—H_2, CO_2, CO, and He—on the structural evolution of Pt nanoparticles, we conducted CO−DRIFTS experiments (Figure S1). These experiments answered the question of whether cooling under a given atmosphere (e.g., CO alone) could induce fragmentation or whether synergistic effects with other gases were required. By monitoring changes in CO spectroscopic signatures, we captured the dynamic restructur-

https://doi.org/10.1021/acscatal.5c06004
ACS Catal. 2025, 15, 19709−19720

ing processes that preceded and/or accompanied the catalyst fragmentation. The DRIFTS spectra in Figure 1a,c show that both Pt single atoms on ceria nano domes supported on ceria (PCC) and titania (PCT) samples, in their as-prepared states, exhibit a distinct band at 2090 cm^{-1}, corresponding to CO adsorbed on isolated ionic Pt single sites.[1,8,9,15,36,46] Upon heating to 300 °C under RWGS conditions, this feature disappears in both samples (Figure 1a–d). Simultaneously, a broader band at 2064 cm^{-1} emerges, attributed to CO adsorption on well-coordinated (WC) sites of metallic Pt clusters.[57,58] Together, these trends indicate aggregation of Pt into larger clusters or nanoparticles. Notably, the observed CO–Pt signals arise solely from in situ–generated CO during RWGS, as no external CO was introduced. These observations are consistent with previous studies, which reported that PCT undergoes complete reduction to metallic Pt at 300 °C, while PCC experiences an almost complete reduction, retaining only a small fraction of ionic Pt species.[8] Although both samples display comparable behavior during high-temperature RWGS reaction conditions, intriguingly, their structural evolution during cooling differs significantly. For the PCC sample (Figure 1c,d), cooling under RWGS conditions followed by CO exposure leads to the reappearance of a sharp 2087 cm^{-1} band, indicative of the reformation of ionic Pt single atoms. A similar high-wavenumber feature is observed when PCC is cooled directly under CO, suggesting an intrinsic propensity for Pt cluster fragmentation into single atoms under both RWGS and CO environments. In contrast, the PCT sample (Figure 1a,b) exhibits a more restrained structural response. After cooling under RWGS conditions and subsequent CO exposure, a narrow 2087 cm^{-1} band emerges (Figure 1a), consistent with partial redispersion into ionic Pt single atoms. However, when PCT is cooled directly under CO from 300 °C to room temperature, no distinct peak near 2087 cm^{-1} is detected (Figure 1b). Instead, the spectrum displays a broad feature shifted to higher wavenumbers, potentially obscuring any subtle contribution from ionic Pt single atoms. To ensure that the difference in CO–DRIFTS features for the PCT sample under RWGS vs CO-cooling was not due to CO coverage, we repeated the CO-cooling experiment using 0.30% CO matching the CO concentration generated during RWGS (0.30 ± 0.05%, measured by mass spectrometry). As shown in Figure S2, the resulting spectrum closely resembled that from 5% CO cooling and lacked the distinct 2087 cm^{-1} peak seen after RWGS cooling, confirming that CO partial pressure alone does not explain the spectral differences. It is essential to note that meaningful comparisons of support effects on the structure and properties of nanoparticles must consider differences in particle size distributions. The average Pt nanoparticle sizes for PCC and PCT samples after aggregation are 1.4 and 1.3 nm[8] with similar distribution widths. In the current work, the PCT sample was remeasured by TEM, and the results (Figure S3) are shown to be in full agreement with our previous work on these same samples.[8] Therefore, these experimental results described below (XAFS and DRIFTS) underscore the support-specific differences in fragmentation behaviors of PCC and PCT.

To further elucidate the influence of RWGS conditions on Pt restructuring within the PCT sample, two controlled experiments were performed (Figure 2). In the first experiment (Figure 2a), the RWGS reaction was interrupted by stopping the H_2 flow, and the sample was cooled under CO_2 before CO exposure at room temperature. Under these conditions, the

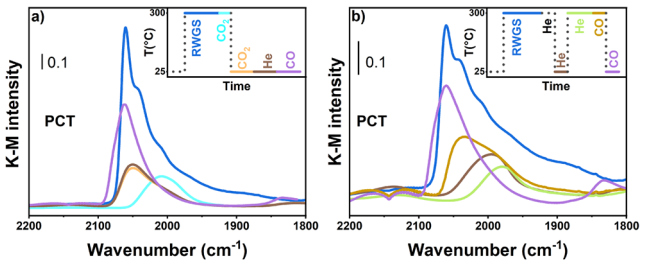


Figure 2. CO–DRIFTS spectra of PCT collected during (a) cooling under CO_2 after RWGS reaction, to contrast with the effect of cooling under RWGS condition (Figure 1a), and during (b) He purge at 300 °C and subsequent CO cooling, to contrast with the effect of RWGS condition at 300 °C (Figure 1b).

characteristic DRIFTS band at 2087 cm^{-1}, corresponding to CO adsorption on ionic Pt single atoms as seen in Figure 1a, was absent. This result indicates that the fragmentation of Pt is not induced merely by CO introduction at room temperature, but rather by the cooling process under RWGS conditions. In the second experiment (Figure 2b), the sample was heated at 300 °C in He instead of under RWGS conditions prior to CO cooling in the second cycle. Under these conditions, the CO-cooling response differs markedly from that observed when preceded by RWGS at 300 °C (Figure 1b), lacking the shift toward high wavenumber and instead producing a peak centered near 2064 cm^{-1}, suggesting a distinctly different restructuring pathway.

The summary of these controlled CO–DRIFTS experiments provides us with several important insights:

1. While CO plays a critical role in driving fragmentation, it alone is insufficient to induce substantial fragmentation in certain systems, such as PCT. As seen from Figure 1b under CO cooling, PCT does not show a distinct high wavenumber peak corresponding to single atoms. Significant fragmentation occurs only under RWGS cooling conditions.
2. PCC and PCT show different fragmentation behavior. Unlike PCT, which undergoes appreciable Pt fragmentation only under RWGS cooling conditions, the PCC sample exhibits signs of redispersion under both CO and RWGS cooling. This disparity emphasizes the critical influence of the support material and the local chemical environment on the dynamics of Pt fragmentation.

These findings support the hypothesis that RWGS conditions promote Pt fragmentation differently than CO alone for systems such as PCT. The explanation of this is "hidden" in the synergistic effects of H_2, CO_2, and/or CO and oxide support on the metal catalyst. We note, as shown earlier, in the case of PCT, aggregation is more favorable due to the migration of Pt nanoparticles toward the ceria–titania interface.[8] This interface environment facilitates aggregation by spatially confining metal species in proximity to each other.[15] Moreover, the high density of oxygen vacancies at the ceria–titania interface serves as anchoring sites.[59–61]

Despite CO–DRIFTS being a powerful technique for probing the fragmentation of metal catalysts due to CO's ability to monitor structural evolution under varying thermal or adsorptive conditions, it presents inherent limitations for being the sole source of information about the fragmentation effects. The dual role of CO, acting both as a probe and a potential driver of metal redispersion, complicates the interpretation of

https://doi.org/10.1021/acscatal.5c06004
ACS Catal. 2025, 15, 19709–19720

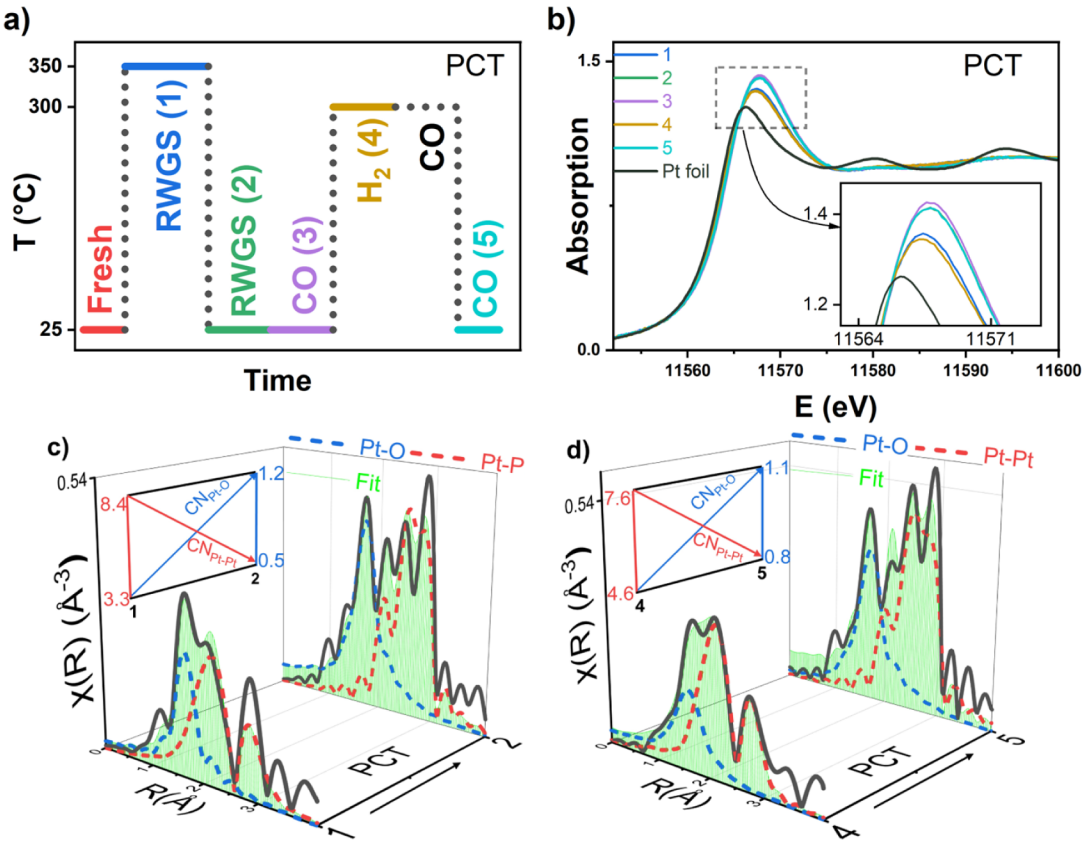


Figure 3. Summary of XANES and EXAFS data and analysis results. (a) Time temperature diagram. (b) Normalized XANES spectra. Fourier transform magnitudes of k^2 -weighted Pt L_3 EXAFS spectra for the data and theoretical fits after cooling in (c) RWGS conditions and (d) after cooling in CO conditions.

spectroscopic (CO−DRIFTS) data. Specifically, the broad high wavenumber feature in Figure 1b for PCT cooled under CO from 300 °C to room temperature lacks a distinct 2087 cm^{-1} feature typically associated with CO bound to ionic Pt single atoms. While this may suggest the absence of isolated Pt species, the broad, high-wavenumber envelope observed could obscure a weak contribution. Implying, very weak redispersion under these conditions cannot be excluded. However, it cannot be unequivocally ascribed to partial reformation of single-atom Pt species; alternative contributions from CO adsorption on terrace-rich metallic domains, such as Pt(111) facets,[58,62] or from electronic perturbations induced by residual hydrogen following RWGS are also plausible.

Additionally, although CO−DRIFTS is exquisitely sensitive to Pt speciation, it is not definitive, as ν(CO) is also influenced by factors such as surface coverage and particle size.[57] For example, larger Pt nanoparticles under high CO coverage exhibited atop-CO bands near 2088 cm^{-1}, in contrast to the 2064 cm^{-1} band observed for our Pt nanoparticles formed under RWGS conditions, rendering simple band-based assignments.[63] Moreover, while DRIFTS excels at detecting surface-adsorbed species, it cannot provide direct, quantitative insights into key structural parameters such as bond lengths, coordination environments, or the extent of metal aggregation and redispersion. We therefore adopt a multimodal strategy combining CO−DRIFTS, XAFS, HAADF-STEM, and theoretical modeling for our investigation.

XAFS-Based Quantification of the Fragmentation Phenomenon in PCT: Comparison of the RWGS vs CO Atmospheres. To overcome DRIFTS limitations, we conducted XAFS experiments in situ. XAFS provided precise bond distances and coordination numbers for Pt−Pt and Pt−O, offering new insights into Pt fragmentation mechanisms. The details of the XAFS study are shown in Figure 3a, featuring the time−temperature profile of the XAFS experiment. The sample is initially heated to 350 °C under RWGS (condition 1), then cooled under the same atmosphere (condition 2) before exposure to CO (condition 3). It is subsequently heated to 300 °C under H_2 to induce reduction (condition 4), followed by exposure to CO at 300 °C, and finally cooled under CO conditions (condition 5). Figure 3b shows the Pt L_3-edge XANES spectra. Under high-temperature conditions using RWGS (condition 1) and pure H_2 (condition 4), the Pt L_3 white line intensity decreases toward that of metallic Pt foil, indicating that dispersed Pt single atoms aggregate into clusters or nanoparticles under these reducing conditions.[8,44,64] Conversely, when the sample is cooled under RWGS (condition 2) or CO (condition 5), the intensity of the white line increases. As cooling is performed in the presence of hydrogen and in the absence of oxygen, partial reoxidation is ruled out, and the increase in intensity is attributed to partial redispersion of the ionic Pt species.[44]

Figure S4c,d presents the R-space Extended X-ray Absorption Fine Structure (EXAFS) spectra acquired under the conditions described in Figure 3a. While qualitative analysis provides initial food for thought, it is insufficient to fully resolve overlapping contributions from thermal and static disorder versus actual structural changes based on the visual examination only. Thus, quantitative fitting was performed to extract structural parameters. Pt EXAFS spectra collected

https://doi.org/10.1021/acscatal.5c06004
ACS Catal. 2025, 15, 19709−19720

before and after cooling under RWGS and CO conditions were analyzed using a model incorporating Pt−O and Pt−Pt single-scattering paths. The R-space data and corresponding fits are shown in Figure 3c,d. Variations in the Pt−O (first peak) and Pt−Pt (second peak) features indicate changes in the local coordination environment. Upon cooling from high-temperature RWGS and CO conditions (conditions 1 and 4) to room temperature (conditions 2 and 5), an increase in the Pt−O peak intensity suggests a greater degree of Pt−O coordination, consistent with partial redispersion into single-atom sites. Notably, although Pt−Pt coordination is higher at elevated temperatures due to aggregation, the peak intensity appears diminished, owing to an increased Debye−Waller factor at high temperature. Quantitative EXAFS fitting results of the Pt L_3-edge spectra are summarized in Table S1, with key trends illustrated in Figure 4. Under high-temperature RWGS conditions (condition 1), the Pt−Pt coordination number (CN) is 8.4 ± 4.0, indicative of extensive clustering.

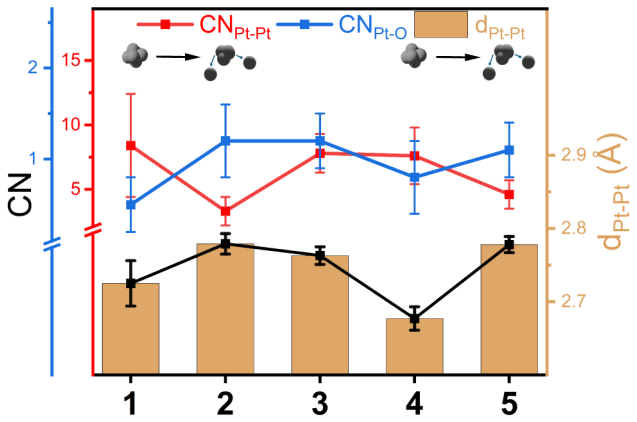


Figure 4. Evolution of Pt−Pt and Pt−O coordination numbers (CN) and average Pt−Pt bond distances.

Upon cooling under the RWGS atmosphere to room temperature (condition 2), the Pt−Pt CN sharply decreases to 3.3 ± 1.1, accompanied by an increase in Pt−O CN from 0.5 ± 0.3 to 1.2 ± 0.4. Although such coordination changes could, in principle, result from nanoparticle flattening,[65] this possibility is excluded based on DRIFTS results (Figure 1a). Specifically, CO probing at room temperature reveals a sharp decline in the 2012 cm^{-1} band associated with under-coordinated (UC) sites, behavior inconsistent with flattening, which would typically increase the UC signal. Heating under H_2 (condition 4) yields a Pt−Pt CN of 7.6 ± 2.2, consistent with particle growth, while cooling under CO (condition 5) results in a moderate decrease of Pt−Pt CN to 4.6 ± 1.1 and a corresponding Pt−O CN increase from 0.8 ± 0.4 to 1.1 ± 0.3. A direct comparison of these trends demonstrates that Pt fragmentation is more pronounced under RWGS cooling than under CO cooling, in agreement with DRIFTS observations. Additionally, the Pt−Pt bond length under RWGS conditions (condition 1) is 2.725 ± 0.031 Å, noticeably longer than that observed after heating under H_2 (condition 4), which is 2.677 ± 0.016 Å. This bond elongation under RWGS conditions is due to hydrogen infiltration and weakening of Pt−Pt interactions.[66] The resulting destabilization likely contributes to the enhanced Pt fragmentation observed under RWGS conditions compared to CO or H_2 alone. A noteworthy caveat is that CO introduction at room temperature (condition 3) induces aggregation, as evidenced by EXAFS results showing an increase in Pt−Pt coordination number (CN) to 7.8 ± 1.5. Additionally, the increased intensity of ∼ 2064 cm^{-1} region (corresponding to CO adsorption on well-coordinated Pt sites) and bridging CO feature at ∼ 1830 cm^{-1} in the DRIFTS spectrum (Figure 1a) further supports CO-induced aggregation. These observations are consistent with prior reports of CO-induced aggregation at room temperature,[24,67,68] reinforcing our finding that the observed Pt fragmentation under RWGS conditions is not attributable to CO exposure at room temperature.

Condition 3 was selected as a reference point to validate the coordination number (CN) analysis derived from EXAFS and size analysis by STEM, as the majority of Pt atoms are expected to reside within nanoparticles under this condition (vide supra). STEM imaging of the same samples following exposure to Conditions 1−3 revealed an average particle diameter of 1.3 nm (Figure S3). Applying the cuboctahedral model described in Supplementary Discussion 1.1, the EXAFS-derived CN corresponded to a particle diameter of 1.4 nm, in excellent agreement with the STEM measurements.[69−72]

To corroborate the DRIFTS and XAFS results, high-angle annular dark-field STEM (HAADF-STEM) was used to follow the structural evolution of Pt in the PCT catalysts (Figure S5). In the as-synthesized material (Figure S5a), there was no evidence of nanoparticle formation. After cooling under RWGS conditions (Figure S5b) and following CO exposure (Figure S5c), both Pt clusters and isolated single atoms became apparent (highlighted by white circles). Notably, the Pt nanoparticles were observed preferentially at the CeO_2−TiO_2 interface.

DFT Insights into Reaction-Driven Pt Fragmentation. To provide further insight into the structural evolution of Pt under reaction conditions, we performed DFT calculations. Two model structures, $CeO_2(100)$ and $Pt_9/CeO_2(100)$, were constructed to describe the CeO_2 nanoparticles observed in the experiment and Pt on CeO_2.[47−56] In our previous study, we found that Pt SA is thermodynamically prone to agglomeration under the RWGS reaction conditions.[8,44] The H-covered CeO_2 surface eventually weakens the interaction between Pt SA and CeO_2, facilitating the surface diffusion of Pt SAs with a relatively low activation barrier energy (E_{act} = 0.90 eV) compared to the pristine surface of CeO_2.[36] Therefore, Pt NPs can be formed on the H-covered $CeO_2(100)$ surface, upon which we subsequently evaluated the reaction mechanism for RWGS. The DFT-calculated binding energy (E_{bind}) shows that the H_2 molecules are strongly adsorbed on Pt_9/H-covered $CeO_2(100)$ compared to CO_2 molecules (Figure S6), indicating that the Pt NPs are more likely to be covered by H_2 than CO_2, in advance. The interfacial sites of $Pt_9/CeO_2(100)$, fully covered by H atoms, exhibit the potential for additional hydrogen spillovers. As H diffuses across the $CeO_2(100)$ surface, it spontaneously reacts with the hydroxyl species in the $CeO_2(100)$ surface, facilitating the formation of H_2O. The formed H_2O exhibits a production energy (E_{prod}) of 1.23 eV and is released from the interfacial region without requiring an activation barrier energy. Given the high operating temperature of the RWGS reaction, such a relatively high E_{prod} of H_2O is likely to be compensated by the entropic contribution to the Gibbs free energy of H_2O desorption (Figure S7). The production of H_2O immediately generates the oxygen vacancy at the interfacial site, where an activation site for the CO_2 molecules is subsequently provided. The E_{bind}

https://doi.org/10.1021/acscatal.5c06004
ACS Catal. 2025, 15, 19709−19720

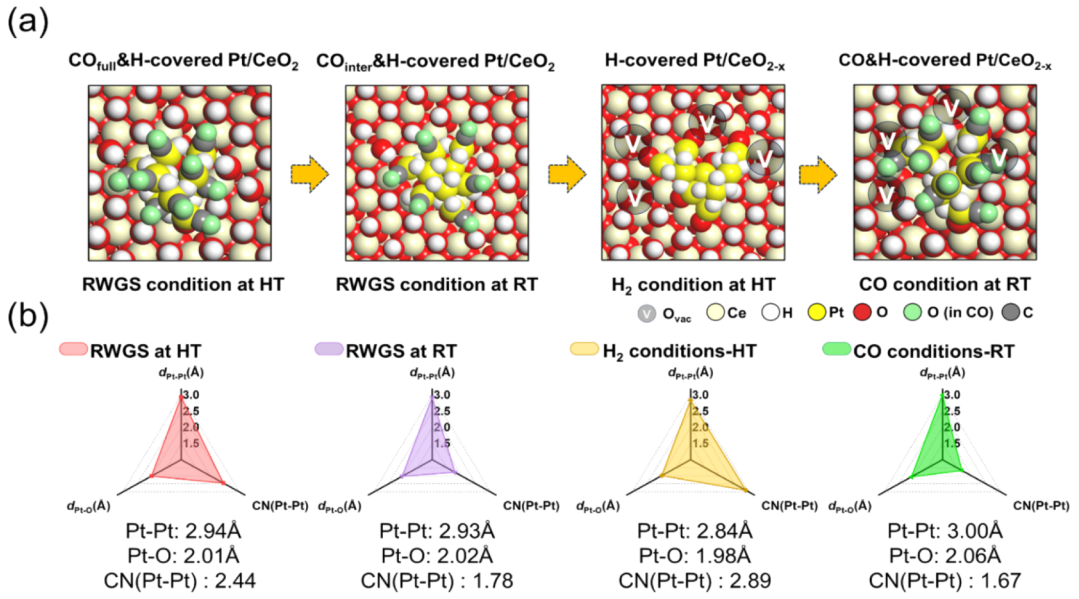


Figure 5. DFT-optimized structures of Pt$_9$/H−CeO$_2$(100) under four reaction conditions: RWGS-HT, RWGS-RT, H$_2$-condition-HT, and CO-condition-RT. (a) Atomic configurations showing adsorbates and oxygen vacancies. (b) Radar plots comparing average Pt−Pt distance, Pt−O distance, and coordination number (CN), highlighting structural changes in the Pt$_9$ cluster depending on temperature and adsorbate environment.

of CO$_2$ (E_{bind} = −0.98 eV) at the oxygen vacancy site indicates that the CO$_2$ is spontaneously activated during the RWGS reaction. Furthermore, the subsequent reverse spillover of CO, formed via CO$_2$ dissociation, is associated with endothermic energetics (E = 1.20 eV), suggesting that CO can be stabilized at the Pt interface site. Considering the high temperatures in the RWGS reaction, reverse spillover of CO onto the Pt nanoparticle is likely to occur occasionally, potentially leading to the release of CO from the less stable sites on the Pt NP surface.

Based on the simplified RWGS reaction energetics (Figure S7), it is expected that under high-temperature conditions, both CO and hydrogen species would extensively cover the Pt nanoparticle surface. Conversely, at lower temperatures, CO is likely to reside predominantly at the interface. To enable a direct comparison with experimentally obtained XAS results (Figure 3), we constructed DFT-based models to represent the experimental conditions. We described the corresponding steady-state configurations under each condition. Accordingly, we constructed the four types of models: fully coadsorbed CO and H on Pt$_9$/H-CeO$_2$(100), coadsorbed CO at the interfacial Pt site and H on Pt$_9$/H-CeO$_2$(100), H-covered Pt$_9$/H-CeO$_{2-x}$, and CO-covered Pt$_9$/H-CeO$_{2-x}$(100), which represent the reaction conditions of RWGS-HT, RWGS-RT, H$_2$-conditions-HT, and CO-conditions-RT, respectively. Figure 5 provides a detailed comparison of Pt$_9$ NP structures under four different reaction environments, focusing on Pt−Pt distances, Pt−O distances, and coordination number (CN). To ensure consistency in the structural analysis, only Pt−Pt pairs with interatomic distances shorter than 3.5 Å were considered when calculating the average Pt−Pt distance and coordination number. This threshold was chosen to reflect meaningful metallic bonding interactions within the Pt nanoparticle.

To clarify the effects of hydrogen and CO and to establish a structural reference, we first analyzed the configurations of Pt$_9$/CeO$_2$, Pt$_9$/H-CeO$_2$, H-covered Pt$_9$/CeO$_2$, and CO-covered Pt$_9$/H-CeO$_2$. As shown in Figure 6, the Pt$_9$/CeO$_2$ and Pt$_9$/H-CeO$_2$ models, where no reactants are adsorbed on the Pt surface, exhibit the most crystalline nanoparticle structures, with the highest CN of 4. Upon exposure to both H$_2$ and CO, the Pt$_9$ cluster undergoes pronounced structural reorganization, reflected by increased Pt−Pt and Pt−O bond lengths relative to the initial Pt$_9$/CeO$_2$ structure. This indicates a relaxation of intracluster bonding alongside a weakened interaction with the ceria support, underscoring the synergistic influence of H$_2$ and CO on the cluster's internal bonding environment.

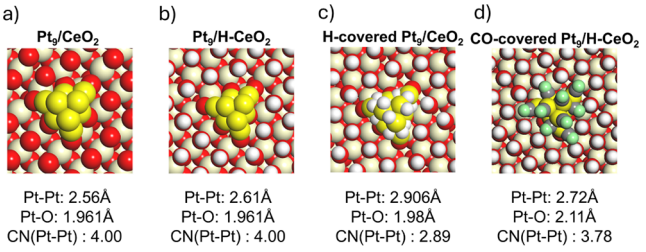


Figure 6. DFT-optimized structures and corresponding physical information on (a) Pt$_9$/CeO$_2$, (b) Pt$_9$/H-CeO$_2$, (c) H-covered Pt$_9$/CeO$_2$, and (d) CO-covered Pt$_9$/H-CeO$_2$.

In the RWGS-HT configuration, where both CO and H are coadsorbed, the CN is relatively high, indicating that Pt atoms retain strong connectivity within the NP. Although H and CO coverage slightly increases the Pt−Pt and Pt−O distances by weakening the metal-support interaction, the overall nanoparticle geometry remains stable and well-coordinated. Under RWGS-RT conditions, where CO adsorption is localized only at the interfacial Pt sites due to limited thermal energy, a decrease in CN is observed, reflecting reduced Pt−Pt coordination near the interface, which may indicate an increased likelihood of Pt nanoparticle fragmentation under these conditions. Simultaneously, the Pt−O distances increased slightly, suggesting that interfacial Pt atoms are experiencing less interaction with the CeO$_2$ surface. Under H$_2$-condition-HT, the Pt−Pt distances are the shortest among all models, and the CN is higher than that of the RWGS-RT

https://doi.org/10.1021/acscatal.5c06004
ACS Catal. 2025, 15, 19709−19720

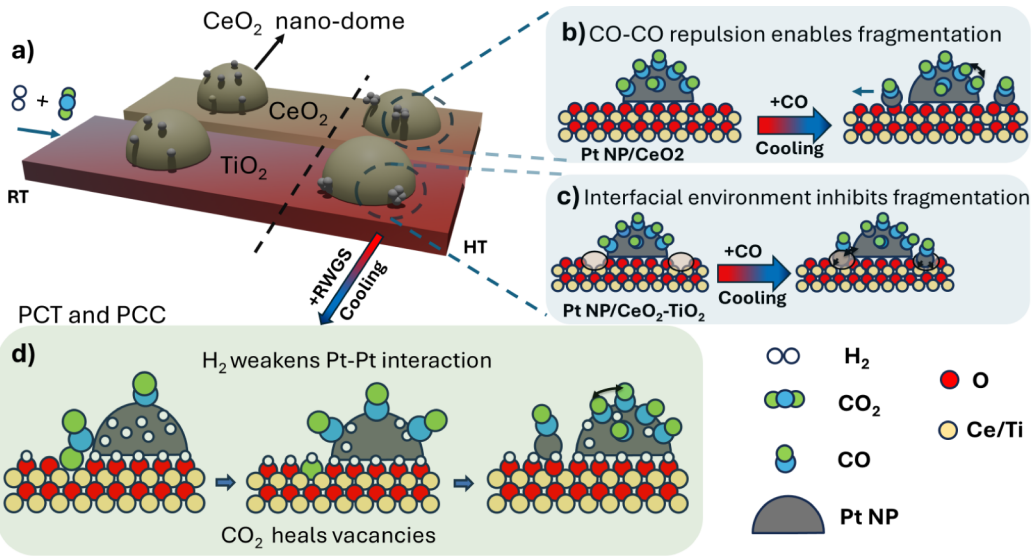


Figure 7. Schematic of Pt nanoparticle evolution. (a) Formation and migration of Pt nanoparticles on CeO_2 and CeO_2−TiO_2 supports with increasing temperature under RWGS condition. (b) Reduced vacancy density on CeO_2 surfaces enables easier Pt fragmentation under CO. (c) Higher vacancy density at CeO_2−TiO_2 interfaces enhances atom pinning and inhibits fragmentation under CO cooling. (d) CO_2 healing of oxygen vacancies and H_2 promotes Pt dispersion for both PCC and PCT.

configuration. These observations indicate that the formation of surface oxygen vacancies, induced by hydrogen spillover, contributes to stabilizing the Pt nanoparticle by reinforcing Pt−Pt connectivity. Furthermore, compared to the vacancy-free H-covered Pt_9/CeO_2 model in Figure 6, where the CN and Pt−O distances remain similar, but the Pt−Pt distance is only slightly higher, it is evident that the presence of vacancies does not significantly promote fragmentation. Instead, vacancies enhance the structural integrity of the nanoparticle under hydrogen-rich conditions. Under CO-rich conditions at room temperature, CO preferentially binds to Pt sites, weakening Pt−O interactions and disrupting Pt−Pt connectivity. This dual effect reflects a diminished interaction of the Pt cluster both with the ceria support and among Pt atoms themselves. In the CO-condition−RT model, although CO is adsorbed on Pt surface, the preexisting oxygen vacancies formed during previous hydrogen treatment suppress the formation of additional products such as H_2O and CO_2. Consequently, both CO and H persist on the Pt surface without undergoing additional transformation. The coordination number (CN) declines compared to those observed under H_2 at high temperature, while both Pt−Pt and Pt−O bond lengths slightly increase, indicating dynamic restructuring of the Pt cluster. Notably, some Pt fragments from the original Pt_9 cluster appear to localize at oxygen vacancies, suggesting that such defects function as anchoring sites (Figure 5).

It is important to note that while the study provides mechanistic insight into Pt fragmentation under RWGS conditions, the specific roles of oxygen vacancies and support reducibility were not the primary focus. The investigation centered on RWGS-induced structural evolution, as examined using the PCC and PCT systems. A more comprehensive understanding of support effects, particularly vacancy-mediated stabilization and redox dynamics, will require future targeted studies. In addition, while previous studies have demonstrated that surface OH species can assist in metal redispersion, primarily under oxidative or hydrothermal conditions,[73−75] we note that, in our system, redispersion occurs under non-oxidative RWGS or CO only environments during the cooling phase. Although transient OH species may contribute to stabilizing atomically dispersed Pt once formed, they are not the primary drivers. Instead, our combined spectroscopic and control experiments indicate that CO mediated interactions, in synergy with H_2 and CO_2, dominate the fragmentation mechanism.

Figure 7 illustrates the contrasting fragmentation behaviors of Pt nanoparticles under CO and RWGS conditions, emphasizing the greater effectiveness of RWGS in promoting fragmentation, particularly in systems such as PCT where Pt nanoparticles preferentially nucleate at the CeO_2 and TiO_2 interface (Figure 7a). Although CO exposure alone can induce repulsive interactions among surface-bound species that weaken Pt to Pt bonds and trigger fragmentation in PCC systems (Figure 7b), these effects are insufficient to overcome the structural constraints imposed by the interfacial environment in PCT (Figure 7c). In PCT, this interface not only presents a high concentration of oxygen vacancies,[59−61] enabling the pinning of transiently mobile Pt atoms, but also spatially confines metal species, favoring aggregation over dispersion.[15] By contrast, RWGS conditions create a more conducive environment for fragmentation, even in such confined systems such as PCT. Here, H_2 infiltration and CO weaken intracluster Pt−Pt bonds and attenuate metal−support interactions, while CO_2 heals oxygen vacancies,[76−78] thereby diminishing the anchoring strength of the interface (Figure 7d). This synergistic interplay among H_2, CO, and CO_2 effectively enables fragmentation to proceed despite interfacial confinement. Whereas conventional catalyst redispersion methods depend on high-temperature oxidative or chlorination treatments,[79] our findings uncover an alternative, low-temperature redispersion pathway.

CONCLUSIONS

This work uncovers a reaction-driven mechanism for catalyst redispersion, wherein Pt nanoparticles fragment into atomically dispersed species during the cooling phase of the reverse water gas shift (RWGS) reaction. Through a combination of

https://doi.org/10.1021/acscatal.5c06004
ACS Catal. 2025, 15, 19709−19720

operando DRIFTS, XAFS, HAADF-STEM, and DFT, we demonstrate that this process is regulated by a synergistic interplay among H_2, CO_2, and CO. The structural evolution of Pt is highly dependent on the local support environment. On ceria, fragmentation readily occurs even under CO alone, whereas on ceria−titania, interfacial confinement and vacancy-mediated pinning suppress redispersion. Under RWGS conditions, however, fragmentation is enabled even in the more constrained PCT system, as hydrogen weakens Pt−Pt interactions and CO_2 heals oxygen vacancies. Our findings resolve the complexity of metal−metal, metal−support, and metal−adsorbate interactions and their roles in dictating restructuring pathways. This mechanistic understanding offers, potentially, a new framework for designing regenerable and sinter-resistant catalysts by leveraging low-temperature, reaction-induced fragmentation as a tool for dynamic catalyst stabilization.

■ ASSOCIATED CONTENT

Supporting Information

The Supporting Information is available free of charge at https://pubs.acs.org/doi/10.1021/acscatal.5c06004.

EXAFS size determination from coordination number; supplementary figures (time−temperature profile, particle size distributions, EXAFS spectra, HAADF-STEM images, DFT binding energies, DFT mechanism); supplementary tables (EXAFS fit results, reaction gas mixtures); supplementary references (PDF)

■ AUTHOR INFORMATION

Corresponding Author

Anatoly I. Frenkel − *Department of Materials Science and Chemical Engineering, Stony Brook University, Stony Brook, New York 11794, United States; Division of Chemistry, Brookhaven National Laboratory, Upton, New York 11973, United States;* orcid.org/0000-0002-5451-1207; Email: anatoly.frenkel@stonybrook.edu

Authors

Rafat H. Aunkon − *Department of Materials Science and Chemical Engineering, Stony Brook University, Stony Brook, New York 11794, United States*

Hyuk Choi − *Department of Materials Science and Engineering, Chungnam National University, Daejeon 34134, Republic of Korea; School of Materials Science and Engineering, Nanyang Technological University, Singapore 639798, Singapore;* orcid.org/0000-0002-7899-2631

Ryuichi Shimogawa − *Mitsubishi Chemical Corporation, Science and Innovation Center, Yokohama 227-8502, Japan*

Haodong Wang − *Department of Chemistry, Stony Brook University, Stony Brook, New York 11794, United States*

Lihua Zhang − *Center for Functional Nanomaterials, Brookhaven National Laboratory, Upton, New York 11973, United States;* orcid.org/0000-0003-3331-2345

Christian Reece − *Rowland Institute at Harvard, Harvard University, Cambridge, Massachusetts 02142, United States;* orcid.org/0000-0002-3626-7546

Yuanyuan Li − *Chemical Sciences Division, Oak Ridge National Laboratory, Oak Ridge, Tennessee 37831, United States;* orcid.org/0000-0003-3074-9672

Hyun You Kim − *Department of Materials Science and Engineering, Chungnam National University, Daejeon 34134, Republic of Korea;* orcid.org/0000-0001-8105-1640

Complete contact information is available at: https://pubs.acs.org/10.1021/acscatal.5c06004

Author Contributions

A.I.F., R.S., and R.H.A. proposed the project and designed the experiments. R.H.A and A.I.F collected XAFS data and analyzed XAFS data. H.W prepared the catalysts. R.H.A. performed in situ DRIFTS measurements under supervision of A.I.F., Y.L., and C.R., H.C. and H.K. conducted DFT calculations. L. Z. conducted HAADF-STEM characterization. R.H.A., H.C. and A.I.F. wrote the manuscript with contributions from all authors.

Funding

A.I.F. acknowledges support of the National Science Foundation grant 2452446. Y.L.'s effort at ORNL was supported by the U.S. Department of Energy, Office of Science, Office of Basic Energy Sciences, Chemical Sciences, Geosciences, and Biosciences Division, Catalysis Science program. H.Y.K acknowledges the financial support by the National Research Foundation of Korea (NRF) grant funded by the Korean government (Ministry of Science and ICT, MSIT) (RS-2023-NR077216), the Basic Science Research Program through the NRF funded by the Ministry of Education (RS-2021-NR060128). C.R. gratefully acknowledges the Rowland Fellowship through the Rowland Institute at Harvard. This research used beamline 7-BM (QAS) of the National Synchrotron Light Source II, a U.S. DOE Office of Science User Facility operated for the DOE Office of Science by Brookhaven National Laboratory under Contract DESC0012704. Beamline operations were supported in part by the Synchrotron Catalysis Consortium (U.S. DOE, Office of Basic Energy Sciences, Grant DE- SC0012335). This research used a Hitachi2700C STEM of the Center for Functional Nanomaterials, which is a U.S. DOE Office of Science Facility, at Brookhaven National Laboratory under Contract DESC0012704.

Notes

The authors declare no competing financial interest.

■ ACKNOWLEDGMENTS

This work is dedicated to the memory of our dear colleague, friend and coauthor, Dr. Haodong Wang. The authors gratefully acknowledge the assistance of Drs. Lu Ma, Nebojsa Marinkovic, Akhil Tayal, and Dali Yang for their support during XAS measurements.

■ ABBREVIATIONS

PCC, Pt on ceria catalyst; **PCT**, Pt on ceria−titania catalyst; **RWGS**, reverse water gas shift; **DRIFTS**, diffuse reflectance infrared Fourier transform spectroscopy; **XAS**, X-ray absorption spectroscopy; **XAFS**, X-ray absorption fine structure; **XANES**, X-ray absorption near edge structure; **EXAFS**, extended X-ray absorption fine structure; **HAADF-STEM**, high-angle annular dark-field scanning transmission electron microscopy; **DFT**, density functional theory; **CN**, coordination number; **NP**, nanoparticle; **UC**, under-coordinated; **WC**, well-coordinated; **E_bind**, binding energy; **E_act**, activation energy; **E_prod**, product formation energy

REFERENCES

(1) Nie, L.; Mei, D.; Xiong, H.; Peng, B.; Ren, Z.; Hernandez, X. I. P.; DeLariva, A.; Wang, M.; Engelhard, M. H.; Kovarik, L.; et al. Activation of Surface Lattice Oxygen in Single-Atom Pt/CeO_2 for Low-Temperature Co Oxidation. *Science* **2017**, *358* (6369), 1419−1423.

(2) Li, X.; Pereira-Hernández, X. I.; Chen, Y.; Xu, J.; Zhao, J.; Pao, C.-W.; Fang, C.-Y.; Zeng, J.; Wang, Y.; Gates, B. C.; et al. Functional CeO_xNanoglues for Robust Atomically Dispersed Catalysts. *Nature* **2022**, *611* (7935), 284−288.

(3) Huang, P.; Huang, J.; Pantovich, S. A.; Carl, A. D.; Fenton, T. G.; Caputo, C. A.; Grimm, R. L.; Frenkel, A. I.; Li, G. Selective CO_2 Reduction Catalyzed by Single Cobalt Sites on Carbon Nitride under Visible-Light Irradiation. *J. Am. Chem. Soc.* **2018**, *140* (47), 16042−16047.

(4) Yan, H.; Cheng, H.; Yi, H.; Lin, Y.; Yao, T.; Wang, C.; Li, J.; Wei, S.; Lu, J. Single-Atom Pd1/Graphene Catalyst Achieved by Atomic Layer Deposition: Remarkable Performance in Selective Hydrogenation of 1,3-Butadiene. *J. Am. Chem. Soc.* **2015**, *137* (33), 10484−10487.

(5) An, Z.; Yang, P.; Duan, D.; Li, J.; Wan, T.; Kong, Y.; Caratzoulas, S.; Xiang, S.; Liu, J.; Huang, L.; et al. Highly Active, Ultra-Low Loading Single-Atom Iron Catalysts for Catalytic Transfer Hydrogenation. *Nat. Commun.* **2023**, *14* (1), 6666.

(6) Li, Y.; Wang, H.; Song, H.; Rui, N.; Kottwitz, M.; Senanayake, S. D.; Nuzzo, R. G.; Wu, Z.; Jiang, D. E.; Frenkel, A. I. Active Sites of Atomically Dispersed Pt Supported on Gd-Doped Ceria with Improved Low Temperature Performance for Co Oxidation. *Chem. Sci.* **2023**, *14* (44), 12582−12588.

(7) Fernández, E.; Liu, L.; Boronat, M.; Arenal, R.; Concepcion, P.; Corma, A. Low-Temperature Catalytic No Reduction with Co by Subnanometric Pt Clusters. *ACS Catal.* **2019**, *9* (12), 11530−11541.

(8) Wang, H.; Shimogawa, R.; Zhang, L.; Ma, L.; Ehrlich, S. N.; Marinkovic, N.; Li, Y.; Frenkel, A. I. Migration and Aggregation of Pt Atoms on Metal Oxide-Supported Ceria Nanodomes Control Reverse Water Gas Shift Reaction Activity. *Commun. Chem.* **2023**, *6* (1), 264.

(9) DeRita, L.; Dai, S.; Lopez-Zepeda, K.; Pham, N.; Graham, G. W.; Pan, X.; Christopher, P. Catalyst Architecture for Stable Single Atom Dispersion Enables Site-Specific Spectroscopic and Reactivity Measurements of Co Adsorbed to Pt Atoms, Oxidized Pt Clusters, and Metallic Pt Clusters on TiO_2. *J. Am. Chem. Soc.* **2017**, *139* (40), 14150−14165.

(10) Yoo, M.; Kang, E.; Choi, H.; Ha, H.; Choi, H.; Choi, J.-S.; Lee, K.-S.; Celestre, R.; Shapiro, D. A.; Park, J. Y.; Kim, C.; Yu, Y.-S.; Kim, H. Y. Enhancing the Inherent Catalytic Activity and Stability of TiO_2 Supported Pt Single-Atoms at Ceox−Tio2 Interfaces. *J. Mater. Chem. A* **2022**, *10* (11), 5942−5952.

(11) Simonsen, S. B.; Chorkendorff, I.; Dahl, S.; Skoglundh, M.; Sehested, J.; Helveg, S. Direct Observations of Oxygen-Induced Platinum Nanoparticle Ripening Studied by in Situ TEM. *J. Am. Chem. Soc.* **2010**, *132* (23), 7968−7975.

(12) Hansen, T. W.; DeLariva, A. T.; Challa, S. R.; Datye, A. K. Sintering of Catalytic Nanoparticles: Particle Migration or Ostwald Ripening? *Acc. Chem. Res.* **2013**, *46* (8), 1720−1730.

(13) Datye, A. K.; Xu, Q.; Kharas, K. C.; McCarty, J. M. Particle Size Distributions in Heterogeneous Catalysts: What Do They Tell Us About the Sintering Mechanism? *Catal. Today* **2006**, *111* (1−2), 59−67.

(14) Chong, F. K.; Anderson, J. A.; Rochester, C. Effects of Regeneration Cycles on Heptane−H 2 Reactions over Pt−Re/Al_2O_3 Catalysts. *Phys. Chem. Chem. Phys.* **2000**, *2* (24), 5730−5736.

(15) Wang, H.; Rui, N.; Senanayake, S. D.; Zhang, L.; Li, Y.; Frenkel, A. I. Tuning the Placement of Pt "Single Atoms" on a Mixed CeO_2−TiO_2 Support. *J. Phys. Chem. C* **2022**, *126* (38), 16187−16193.

(16) O'Neill, B. J.; Jackson, D. H.; Lee, J.; Canlas, C.; Stair, P. C.; Marshall, C. L.; Elam, J. W.; Kuech, T. F.; Dumesic, J. A.; Huber, G. W. Catalyst Design with Atomic Layer Deposition. *ACS Catal.* **2015**, *5* (3), 1804−1825.

(17) Pan, X.; Bao, X. The Effects of Confinement inside Carbon Nanotubes on Catalysis. *Acc. Chem. Res.* **2011**, *44* (8), 553−562.

(18) Wang, G.; Xu, S.; Wang, L.; Liu, Z.; Dong, X.; Wang, L.; Zheng, A.; Meng, X.; Xiao, F.-S. Fish-in-Hole: Rationally Positioning Palladium into Traps of Zeolite Crystals for Sinter-Resistant Catalysts. *Chem. Commun.* **2018**, *54* (26), 3274−3277.

(19) An, B.; Zhang, J.; Cheng, K.; Ji, P.; Wang, C.; Lin, W. Confinement of Ultrasmall Cu/ZnO $_x$ Nanoparticles in Metal−Organic Frameworks for Selective Methanol Synthesis from Catalytic Hydrogenation of CO_2. *J. Am. Chem. Soc.* **2017**, *139* (10), 3834−3840.

(20) Wang, L.; Wang, L.; Meng, X.; Xiao, F. S. New Strategies for the Preparation of Sinter-Resistant Metal-Nanoparticle-Based Catalysts. *Adv. Mater.* **2019**, *31* (50), 1901905.

(21) Susu, A.; Ogogo, E.; Ngomo, H. The Effect of Sintering-Redispersion on the Selective Aromatic Yield on Supported Platinum Catalysts. *Chem. Eng. Res. Des.* **2006**, *84* (8), 664−676.

(22) Tanabe, T.; Nagai, Y.; Dohmae, K.; Sobukawa, H.; Shinjoh, H. Sintering and Redispersion Behavior of Pt on Pt/MgO. *J. Catal.* **2008**, *257* (1), 117−124.

(23) D'Aniello, M. J., Jr; Monroe, D. R.; Carr, C. J.; Krueger, M. H. The Redispersion of Sintered Pt, Rh, and PtRh Catalysts. *J. Catal.* **1988**, *109* (2), 407−422.

(24) Newton, M. A.; Belver-Coldeira, C.; Martínez-Arias, A.; Fernández-García, M. Dynamic in Situ Observation of Rapid Size and Shape Change of Supported Pd Nanoparticles during Co/No Cycling. *Nat. Mater.* **2007**, *6* (7), 528−532.

(25) Ito, S.-I.; Ishiguro, S.; Kunimori, K. Co Hydrogenation over a Rhodium Vanadate Catalyst: Reduction and Regeneration of $RhVO_4$ on SiO_2. *Catal. Today* **1998**, *44* (1−4), 145−149.

(26) Bernal, S.; Calvino, J.; Cauqui, M.; Omil, J. P.; Pintado, J.; Rodrıguez-Izquierdo, J. Image Simulation and Experimental Hrem Study of the Metal Dispersion in Rh/CeO_2 Catalysts. Influence of the Reduction/Reoxidation Conditions. *Appl. Catal., B* **1998**, *16* (2), 127−138.

(27) Lambrou, P. S.; Polychronopoulou, K.; Petallidou, K. C.; Efstathiou, A. M. Oxy-Chlorination as an Effective Treatment of Aged Pd/CeO_2-Al_2O_3 Catalysts for Pd Redispersion. *Appl. Catal., B* **2012**, *111*, 349−359.

(28) Arteaga, G. J.; Anderson, J. A.; Rochester, C. H. Effects of Oxidation−Reduction and Oxychlorination−Reduction Cycles on Co Adsorption by Pt−Sn/Al_2O_3 catalysts. *J. Catal.* **1999**, *184* (1), 268−279.

(29) Adler, S. F.; Keavney, J. J. The Physical Nature of Supported Platinum. *J. Phys. Chem.* **1960**, *64* (2), 208−212.

(30) Adamiec, J.; Szymura, J.; Wanke, S. S. Poisoning and Regeneration of Pt/MgO. *Stud. Surf. Sci. Catal.* **1993**, *75*, 1405−1418.

(31) Monzón, A.; Garetto, T. F.; Borgna, A. Sintering and Redispersion of Pt/Γ-Al_2O_3 Catalysts: A Kinetic Model. *Appl. Catal., A* **2003**, *248* (1−2), 279−289.

(32) Lieske, H.; Lietz, G.; Spindler, H.; Völter, J. Reactions of Platinum in Oxygen-and Hydrogen-Treated Ptγ-Al_2O_3 Catalysts: I. Temperature-Programmed Reduction, Adsorption, and Redispersion of Platinum. *J. Catal.* **1983**, *81* (1), 8−16.

(33) Yan, G.; Tang, Y.; Li, Y.; Li, Y.; Nguyen, L.; Sakata, T.; Higashi, K.; Tao, F. F.; Sautet, P. Reaction Product-Driven Restructuring and Assisted Stabilization of a Highly Dispersed Rh-on-Ceria Catalyst. *Nat. Catal.* **2022**, *5* (2), 119−127.

(34) Matsubu, J. C.; Yang, V. N.; Christopher, P. Isolated Metal Active Site Concentration and Stability Control Catalytic CO_2 Reduction Selectivity. *J. Am. Chem. Soc.* **2015**, *137* (8), 3076−3084.

(35) Schroeder, E. K.; Hong, S.; Chen, X.; Hoffman, A. S.; Chen, Z.; Khan, A.; Barber, G. D.; Bac, S.; Rioux, R. M.; Yang, J.; et al. Structural Evolution and Stability of Rh/Tio2 Catalysts under CO_2 Hydrogenation Conditions: Influence of the Initial Rh Structure. *ACS Catal.* **2025**, *15* (14), 12133−12147.

(36) Wang, H.; Choi, H.; Shimogawa, R.; Li, Y.; Zhang, L.; Kim, H. Y.; Frenkel, A. I. Unravelling the Origin of Reaction-Driven

https://doi.org/10.1021/acscatal.5c06004
ACS Catal. 2025, 15, 19709−19720

Aggregation and Fragmentation of Atomically Dispersed Pt Catalyst on Ceria Support. *Nanoscale* **2024**, *16* (31), 14716−14721.
(37) Kolb, D. Reconstruction Phenomena at Metal-Electrolyte Interfaces. *Prog. Surf. Sci.* **1996**, *51* (2), 109−173.
(38) Wei, H.; Xie, K.; Zhang, J.; Zhang, Y.; Wang, Y.; Qin, Y.; Cui, J.; Yan, J.; Wu, Y. In Situ Growth of Nixcu1-X Alloy Nanocatalysts on Redox-Reversible Rutile (Nb, Ti)O_4 Towards High-Temperature Carbon Dioxide Electrolysis. *Sci. Rep.* **2014**, *4* (1), 5156.
(39) Weng, Z.; Liu, W.; Yin, L.-C.; Fang, R.; Li, M.; Altman, E. I.; Fan, Q.; Li, F.; Cheng, H.-M.; Wang, H. Metal/Oxide Interface Nanostructures Generated by Surface Segregation for Electrocatalysis. *Nano Lett.* **2015**, *15* (11), 7704−7710.
(40) Eren, B.; Zherebetskyy, D.; Patera, L. L.; Wu, C. H.; Bluhm, H.; Africh, C.; Wang, L.-W.; Somorjai, G. A.; Salmeron, M. Activation of Cu (111) Surface by Decomposition into Nanoclusters Driven by Co Adsorption. *Science* **2016**, *351* (6272), 475−478.
(41) Karaiskakis, A. N.; Biddinger, E. J. Evaluation of the Impact of Surface Reconstruction on Rough Electrodeposited Copper-Based Catalysts for Carbon Dioxide Electroreduction. *Energy Technol.* **2017**, *5* (6), 901−910.
(42) Irvine, J. T.; Neagu, D.; Verbraeken, M. C.; Chatzichristodoulou, C.; Graves, C.; Mogensen, M. B. Evolution of the Electrochemical Interface in High-Temperature Fuel Cells and Electrolysers. *Nat. Energy* **2016**, *1* (1), 15014.
(43) Hu, X.; Xu, D.; Jiang, J. Strong Metal-Support Interaction between Pt and TiO_2 over High-Temperature CO_2 Hydrogenation. *Angew. Chem., Int. Ed.* **2025**, *137* (7), No. e202419103.
(44) Wang, H.; Choi, H.; Shimogawa, R.; Li, Y.; Zhang, L.; Kim, H. Y.; Frenkel, A. I. Unravelling the Origin of Reaction-Driven Aggregation and Fragmentation of Atomically Dispersed Pt Catalysts on Ceria Support. *Nanoscale* **2024**, *16*, 14716−14721.
(45) Chen, C.; Chen, J.-L.; Feng, L.; Hu, J.; Chai, X.; Liu, J.-X.; Li, W.-X. Reactant-Induced Dynamic Stabilization of Highly Dispersed Pt Catalysts on Ceria Dictating the Reactivity of Co Oxidation. *ACS Catal.* **2024**, *14* (5), 3504−3513.
(46) Kottwitz, M.; Li, Y.; Palomino, R. M.; Liu, Z.; Wang, G.; Wu, Q.; Huang, J.; Timoshenko, J.; Senanayake, S. D.; Balasubramanian, M.; Lu, D.; Nuzzo, R. G.; Frenkel, A. I. Local Structure and Electronic State of Atomically Dispersed Pt Supported on Nanosized CeO_2. *ACS Catal.* **2019**, *9* (9), 8738−8748.
(47) Perdew, J. P.; Wang, Y. Accurate and Simple Analytic Representation of the Electron-Gas Correlation-Energy. *Phys. Rev. B* **1992**, *45* (23), 13244−13249.
(48) Kresse, G.; Furthmuller, J. Efficient Iterative Schemes for Ab Initio Total-Energy Calculations Using a Plane-Wave Basis Set. *Phys. Rev. B* **1996**, *54* (16), 11169−11186.
(49) Perdew, J. P.; Burke, K.; Ernzerhof, M. Generalized Gradient Approximation Made Simple. *Phys. Rev. Lett.* **1996**, *77* (18), 3865.
(50) Dudarev, S. L.; Botton, G. A.; Savrasov, S. Y.; Humphreys, C. J.; Sutton, A. P. Electron-Energy-Loss Spectra and the Structural Stability of Nickel Oxide: An LSDA+U Study. *Phys. Rev. B* **1998**, *57* (3), 1505−1509.
(51) Ren, Y.; Tang, Y.; Zhang, L.; Liu, X.; Li, L.; Miao, S.; Sheng Su, D.; Wang, A.; Li, J.; Zhang, T. Unraveling the Coordination Structure-Performance Relationship in Pt1/Fe_2O_3 Single-Atom Catalyst. *Nat. Commun.* **2019**, *10* (1), 4500.
(52) Yoo, M.; Yu, Y.-S.; Ha, H.; Lee, S.; Choi, J.-S.; Oh, S.; Kang, E.; Choi, H.; An, H.; Lee, K.-S.; Park, J. Y.; Celestre, R.; Marcus, M. A.; Nowrouzi, K.; Taube, D.; Shapiro, D. A.; Jung, W.; Kim, C.; Kim, H. Y. A Tailored Oxide Interface Creates Dense Pt Single-Atom Catalysts with High Catalytic Activity. *Energy Environ. Sci.* **2020**, *13* (4), 1231−1239.
(53) Kim, H. Y.; Hybertsen, M. S.; Liu, P. Controlled Growth of Ceria Nanoarrays on Anatase Titania Powder: A Bottom-up Physical Picture. *Nano Lett.* **2017**, *17* (1), 348−354.
(54) Blochl, P. E. Projector Augmented-Wave Method. *Phys. Rev. B* **1994**, *50* (24), 17953−17979.
(55) Henkelman, G.; Uberuaga, B. P.; Jonsson, H. A Climbing Image Nudged Elastic Band Method for Finding Saddle Points and Minimum Energy Paths. *J. Chem. Phys.* **2000**, *113* (22), 9901−9904.
(56) Henkelman, G.; Jónsson, H. Improved Tangent Estimate in the Nudged Elastic Band Method for Finding Minimum Energy Paths and Saddle Points. *J. Chem. Phys.* **2000**, *113* (22), 9978−9985.
(57) Kale, M. J.; Christopher, P. Utilizing Quantitative in Situ Ftir Spectroscopy to Identify Well-Coordinated Pt Atoms as the Active Site for CO Oxidation on Al_2O_3-Supported Pt Catalysts. *ACS Catal.* **2016**, *6* (8), 5599−5609.
(58) Kim, T.-S.; O'Connor, C. R.; Reece, C. Interrogating Site Dependent Kinetics over SiO_2-Supported Pt Nanoparticles. *Nat. Commun.* **2024**, *15* (1), 2074.
(59) Chen, C.-S.; Chen, T.-C.; Wu, H.-C.; Wu, J.-H.; Lee, J.-F. The Influence of Ceria on Cu/TiO_2 Catalysts to Produce Abundant Oxygen Vacancies and Induce Highly Efficient CO Oxidation. *Catal. Sci. Technol.* **2020**, *10* (13), 4271−4281.
(60) Mosrati, J.; Abdel-Mageed, A. M.; Vuong, T. H.; Grauke, R.; Bartling, S.; Rockstroh, N.; Atia, H.; Armbruster, U.; Wohlrab, S.; Rabeah, J.; et al. Tiny Species with Big Impact: High Activity of Cu Single Atoms on CeO_2−TiO_2 Deciphered by Operando Spectroscopy. *ACS Catal.* **2021**, *11* (17), 10933−10949.
(61) Vuong, T. H.; Radnik, J. R.; Rabeah, J.; Bentrup, U.; Schneider, M.; Atia, H.; Armbruster, U.; Grünert, W.; Brückner, A. Efficient Vo_x/Ce_{1-x} Ti_x O_2 Catalysts for Low-Temperature NH_3-SCR: Reaction Mechanism and Active Sites Assessed by in Situ/Operando Spectroscopy. *ACS Catal.* **2017**, *7* (3), 1693−1705.
(62) Lentz, C.; Jand, S. P.; Melke, J.; Roth, C.; Kaghazchi, P. Drifts Study of CO Adsorption on Pt Nanoparticles Supported by DFT Calculations. *J. Mol. Catal. A: Chem.* **2017**, *426*, 1−9.
(63) Ge, S.; Fan, W.; Tang, X.; Cui, Y.; Wang, D.; Gong, X.-Q.; Dai, S.; Lou, Y.; Tang, J.; Guo, Y.; et al. Revealing the Size Effect of Ceria Nanocube-Supported Platinum Nanoparticles in Complete Propane Oxidation. *ACS Catal.* **2024**, *14* (4), 2532−2544.
(64) Wang, H.; Kottwitz, M.; Rui, N.; Senanayake, S. D.; Marinkovic, N.; Li, Y.; Nuzzo, R. G.; Frenkel, A. I. Aliovalent Doping of CeO_2 Improves the Stability of Atomically Dispersed Pt. *ACS Appl. Mater. Interfaces* **2021**, *13* (44), 52736−52742.
(65) McKenna, K. P.; Shluger, A. L. Shaping the Morphology of Gold Nanoparticles by CO Adsorption. *J. Phys. Chem. C* **2007**, *111* (51), 18848−18852.
(66) Liu, G.; Zhou, W.; Ji, Y.; Chen, B.; Fu, G.; Yun, Q.; Chen, S.; Lin, Y.; Yin, P.-F.; Cui, X. Hydrogen-Intercalation-Induced Lattice Expansion of Pd@ Pt Core−Shell Nanoparticles for Highly Efficient Electrocatalytic Alcohol Oxidation. *J. Am. Chem. Soc.* **2021**, *143* (29), 11262−11270.
(67) Chaabane, N.; Lazzari, R.; Jupille, J.; Renaud, G.; Avellar Soares, E. CO-Induced Scavenging of Supported Pt Nanoclusters: A Gisaxs Study. *J. Phys. Chem. C* **2012**, *116* (44), 23362−23370.
(68) Berko, A.; Szökő, J.; Solymosi, F. Effect of CO on the Morphology of Pt Nanoparticles Supported on TiO_2 (1 1 0)-(1× N). *Surf. Sci.* **2004**, *566*, 337−342.
(69) Frenkel, A. I. Applications of Extended X-Ray Absorption Fine-Structure Spectroscopy to Studies of Bimetallic Nanoparticle Catalysts. *Chem. Soc. Rev.* **2012**, *41* (24), 8163−8178.
(70) Frenkel, A. I.; Yevick, A.; Cooper, C.; Vasic, R. Modeling the Structure and Composition of Nanoparticles by Extended X-Ray Absorption Fine-Structure Spectroscopy. *Annu. Rev. Anal. Chem.* **2011**, *4* (1), 23−39.
(71) Montejano-Carrizales, J.; Aguilera-Granja, F.; Moran-Lopez, J. Direct Enumeration of the Geometrical Characteristics of Clusters. *Nanostruct. Mater.* **1997**, *8* (3), 269−287.
(72) Li, Y.; Zakharov, D.; Zhao, S.; Tappero, R.; Jung, U.; Elsen, A.; Baumann, P.; Nuzzo, R. G.; Stach, E.; Frenkel, A. Complex Structural Dynamics of Nanocatalysts Revealed in Operando Conditions by Correlated Imaging and Spectroscopy Probes. *Nat. Commun.* **2015**, *6* (1), 7583.
(73) Lei, H.; Zhang, N.; Hu, S.; Peng, F.; Zhou, J.; He, J.; Zhang, L.; Wang, H.; Ma, C.; Yan, H.; et al. Thermally Triggered Redox

Flexibility of Pt/CeO_2 Cluster Catalyst against in-Situ Atomic Redispersion. *Angew. Chem. Int. Ed.* **2025**, *64* (31), No. e202509239.
(74) Wu, M.-Y.; Li, S.-Q.; Wang, W.-W.; Jia, C.-J. Synergistic Effects of Complex Cu Species in Cu−MgO Catalysts for the Water Gas Shift Reaction. *ACS Catal.* **2024**, *14* (18), 13723−13735.
(75) Jeong, H.; Bae, J.; Han, J. W.; Lee, H. Promoting Effects of Hydrothermal Treatment on the Activity and Durability of Pd/CeO_2 Catalysts for Co Oxidation. *ACS Catal.* **2017**, *7* (10), 7097−7105.
(76) Kattel, S.; Yan, B.; Chen, J. G.; Liu, P. CO_2 Hydrogenation on Pt, Pt/SiO_2 and Pt/TiO_2: Importance of Synergy between Pt and Oxide Support. *J. Catal.* **2016**, *343*, 115−126.
(77) Wang, Y.; Arandiyan, H.; Scott, J.; Aguey-Zinsou, K.-F.; Amal, R. Single Atom and Nanoclustered Pt Catalysts for Selective CO_2 Reduction. *ACS Appl. Energy Mater.* **2018**, *1* (12), 6781−6789.
(78) Goguet, A.; Meunier, F.; Breen, J.; Burch, R.; Petch, M.; Ghenciu, A. F. Study of the Origin of the Deactivation of a Pt/CeO_2 Catalyst during Reverse Water Gas Shift (RWGS) Reaction. *J. Catal.* **2004**, *226* (2), 382−392.
(79) Morgan, K.; Goguet, A.; Hardacre, C. Metal Redispersion Strategies for Recycling of Supported Metal Catalysts: A Perspective. *ACS Catal.* **2015**, *5*, 3430−3445.



https://doi.org/10.1021/acscatal.5c06004
ACS Catal. 2025, 15, 19709−19720